

Automatic selection of focal lengths in a Depth From Defocus measurement system based on liquid lenses



Simone Pasinetti^{a,*}, Ileana Bodini^a, Matteo Lancini^b, Franco Docchio^b, Giovanna Sansoni^a

^a Dept. of Information Engineering (DII), University of Brescia, Brescia, Italy

^b Dept. of Mechanical and Industrial Engineering (DIMI), University of Brescia, Brescia, Italy

ARTICLE INFO

Keywords:

Depth From Defocus
Liquid lenses
Shape measurement
Image processing
Calibration
Phase modulation

ABSTRACT

A simple and compact Depth-From-Defocus (DFD) setup, using telecentric illumination and liquid-lens based camera observation, was shown to perform well for 3D shape acquisition over extended measuring range. A further step to ameliorate the system performance is described in this paper. We focused on finding an algorithm to speed up the calibration step of the method, that automatically determines the minimum number of focal lengths to be used in the calibration and measurement procedure. As a result, the calibration is significantly shortened (up to 80% with respect to the original procedure), and the need to manually (and to some extent arbitrarily) select the focal length pairs is overcome. Measurement errors down to 0.73 mm over the measurement depth range of 130 mm, corresponding to 0.55% of the depth range are achieved, in total agreement with the original system.

1. Introduction

Optical techniques for the 3D acquisition of free forms in space are today very popular, for quite a number of applications. Some of them are based on fringe projection [1–5], whereas some others are based on different techniques such as structured light projection [6–8], multi-frequency projection [9–12], and color-coded pattern projection [13,14]. Such techniques are usually based on optical triangulation layouts, which suffer from typical problems of stereo vision systems such as occlusions and shadows. Coaxial techniques based on Depth From Defocus (DFD) algorithms are emerging as a way to acquire objects without problems that makes the usual stereo vision processes problematic [15–17]. DFD can be either passive (the illumination is provided by the outdoor environment) or active (the illumination is texturized, with fringes of different spatial frequency). The latter systems are so far more performing. However, a general problem of DFD systems is their relatively low depth of field, due to the use of fixed objectives. Setups proposed in the past to compensate for this drawback and to produce extended range systems suffer from an excessive hardware complexity. For example, in [16] and [17], the projection system was duplicated: two sinusoidal gratings oriented perpendicularly to each other are projected on the scene and imaged on a single camera. The gratings are focused at different distances from the lens image plane, resulting in a pair of partially overlapped contrast curves. The extension of the measurement range is achieved by combining the

monotonic rising side of the former with the monotonic falling side of the latter. In [18], the extension of the measurement range is achieved using two camera and two different contrast curves. As in [16] and [17], the monotonic sides of the two contrast curves are used to compute the depth information. Another solution to the extension of the depth range is described in [19], where motor-driven optical zooms were used in the camera or in the projector, which replace the multi-camera or multi-pattern approach.

The presence of commercial liquid lenses with excellent optical quality, as proved in [20], suggested us to apply them as a way to extend the depth range of a DFD measurement without increasing the hardware complexity. In [21] we firstly described a DFD setup making use of a liquid lens objective with fast, voltage controlled, focal length variations. The system has a coaxial illumination/detection geometry: a structured-light, telecentric projection, ensuring a sufficient depth of field, is coupled to a non-telecentric, liquid lens objective connected to the detector, through a beam splitter. The reduced detection depth of field is corrected by adjusting the focal length of the objective, i.e. by controlling the liquid lens. For each objective setting, a contrast curve is obtained over the corresponding depth range. Multiple contrast curve (each corresponding to a lens setting) result in an extended measurement range. In the previous version of the system, two depth measurements have been proposed: (i) an Intensity Contrast Measurement (ICM), acting on a couple of contrast curves covering two adjacent depth sub-ranges, and (ii) a Differential Contrast Measurement (DCM),

* Correspondence to: Dept. of Industrial Engineering, University of Brescia, Via Branze, 38, I-23123, Brescia (BS), Italy.
E-mail address: simone.pasinetti@unibs.it (S. Pasinetti).

combining pairs of contrast curves in a differential curve. A suitable choice of several differential curves covering adjacent depth ranges makes it possible to further extend the depth range with respect to ICM.

Although the results obtained were already encouraging, we found that the system could benefit from further refinements. In particular, we focused on finding a method to speed up the calibration step of the DCM method, which consists in finding the relation among each object position, the focal lengths and the contrast curves over the whole measurement range. To this aim, we worked at an optimization algorithm that automatically determines the focal length pairs to be used in the DCM method and minimizes their number. As a result, the DCM calibration is significantly shortened, and the need to manually (and to some extent arbitrarily) select the focal length pairs is overcome.

In the paper, we will describe the algorithm in detail, highlighting the benefits that it produces in the improvement of the DFD system performances.

2. Description of the system

2.1. Measurement principle

The DFD method implemented in the DCM approach is based on the optical geometry shown in Fig. 1, where the thin lens approximation is used.

The liquid lens objective has an effective focal length F and a diameter D . Points $P_1(x_p, y_p)$ and $P_2(x_p, y_p)$ are two points in the object plane, located at distances S_1 and S_2 from the liquid lens respectively. Their in-focus images both form at point P' , on the image plane, at distance U from the lens, for two different values of focal length, denoted by F_1 and F_2 respectively. Considering an object point P at distance S_p from the lens, its image blurs in a circle of confusion of diameter d . The circle diameter varies depending on the value of the focal length. As shown in the figure, d equals d_1 for $F=F_1$, and d_2 for $F=F_2$. The diameter d can be expressed as a function of the focal lengths, by means of the following expression [22]:

$$d_r = U \cdot D \cdot \left(\frac{1}{F_r} - \frac{1}{S_p} - \frac{1}{U} \right) \quad (1)$$

where D is the lens diameter and parameter r indexes the focal lengths.

In our system, the intensity distribution within the blur circle is described by contrast curves derived by using an active method, based on the projection of fringes of spatial frequency ω_s , their phase shift and their elaboration by means of the modulation measurement profilometry (MMP) approach proposed in [23]. The resulting expression for the contrast C_r is as follows:

$$C_r(i, j) = C_0(i, j) \cdot e^{-\frac{1}{2} \left(\frac{\omega_p}{2\pi} \right)^2 \cdot \sigma_r^2} \quad (2)$$

where (i, j) are the image plane coordinates relative to the circle of confusion center, C_0 is the in-focus contrast of the projected fringes, and σ_r is the spread parameter, directly proportional to the circle of confusion diameter d_r :

$$\sigma_r = k \cdot d_r \quad (3)$$

The proportionality constant k in Eq. (3) is characteristic of the optical system and can be experimentally determined [24]. Parameter ω_p represents the frequency of the fringes at the image plane:

$$\omega_p = \omega_s \cdot \frac{S_p}{U} \quad (4)$$

By combining Eqs. (1), (3), and (4) into Eq. (2), it is possible to measure the distance S_p by measuring the contrast C_r .

2.2. Optical setup

The optical set-up of the system is shown in Fig. 2: it consists of a projection system and of an acquisition system. The former is an LCD projector equipped with a telecentric objective which generates Ronchi fringes used in the phase-shift procedure. The latter is a camera equipped with the liquid lens objective. The camera is an *IDS UI-1540SE*, with a resolution of 1280×1024 pixels and a pixel size of $5.2 \mu\text{m}$. The liquid lens objective is a *Varioptic Caspian C-39-NO*, with an effective focal length F of 16 mm and a diameter D of 11 mm. The optical powers span the interval from -15 to $+27$ Diopters, as a function of the supply voltage from $V_{MIN} = 25$ V (minimum optical power) to $V_{MAX} = 70$ V (maximum optical power). To avoid errors due to the presence of occlusions and shadows, the projection and the acquisition systems are made coaxial by means of a beam splitter placed after them. The field of view is 30×35 mm, while the depth measurement ranges from 87 mm to 227 mm.

During calibration, a white target plane is positioned at a known distance S_p from the objective liquid lens. Then, the objective focal length is set at a given value F_r , a series of images are taken by projecting the phase-shifted fringes on the target, and the contrast C_r is computed. The procedure is repeated for a suitable number of focal lengths N_r , by varying the liquid lens voltage control. The position of the plane is then changed to cover the whole measurement range M_R at equal steps Δ_S , and the above procedure is repeated at each position.

Typical values of N_r , M_R , and Δ_S are 19, 140 mm, and 2.5 mm respectively: a sub-set of contrast C_r curves, computed using the above values, is illustrated in Fig. 3 [21], for a depth range from 87 mm to 227 mm, in steps of 2.5 mm. The curves are bell-shaped, with their maximum value in correspondence to increasing values of depth, for increasing values of focal lengths, in accordance with the optical geometry shown in Fig. 1.

During the measurement, the unknown object position S_p is obtained from the calibration C_r curves. To avoid ambiguity in the

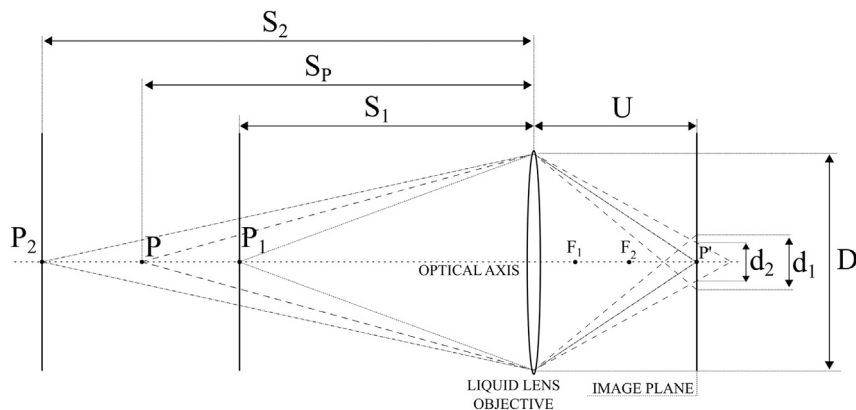


Fig. 1. Geometry of the image formation.

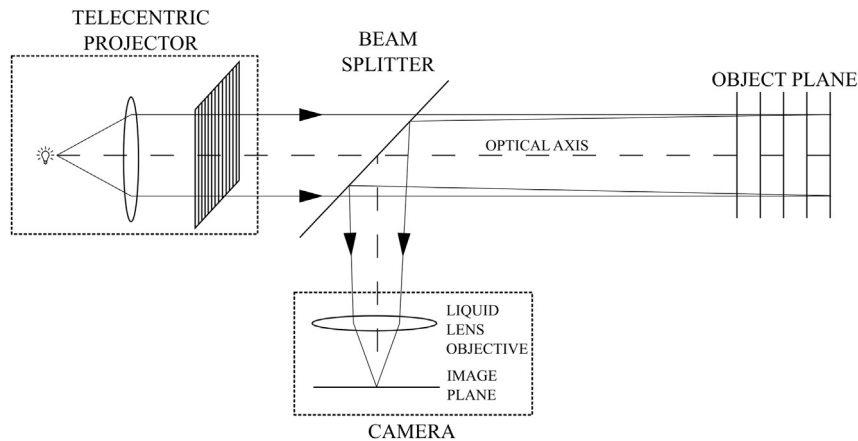


Fig. 2. Optical layout of the system.

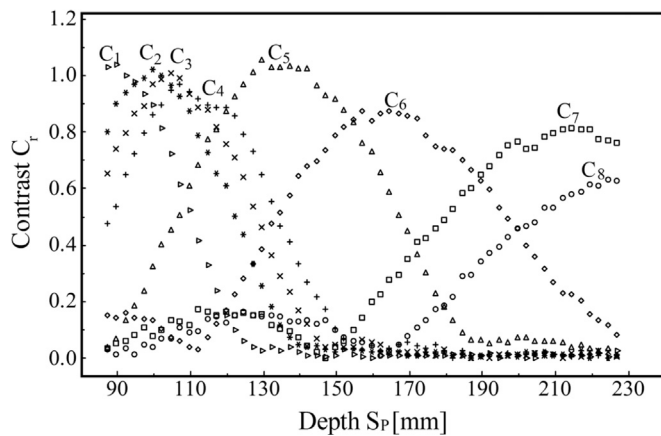


Fig. 3. Experimental values of the contrast C_r as a function of S_p for different values F_i of F . C_1 : $F_1 = 13.60$ mm; C_2 : $F_2 = 13.79$ mm; C_3 : $F_3 = 13.88$ mm; C_4 : $F_4 = 13.98$ mm; C_5 : $F_5 = 14.29$ mm; C_6 : $F_6 = 14.60$ mm; C_7 : $F_7 = 14.93$ mm; C_8 : $F_8 = 15.05$ mm.

measurement of the object position through the contrast value, an additional set of curves is derived from the calibration curves, defined as follows [21]:

$$Q_l^m = \frac{C_l - C_m}{C_l + C_m} \quad (5)$$

In Eq. (5), C_l and C_m are any pair of partially overlapping curves among the contrast curves. Q_l^m , by definition, are monotonic: their value ranges between -1 and $+1$, being zero when C_l and C_m have the same non-zero value, and ± 1 when one of them is zero. Although a single Q_l^m curve could non-ambiguously cover the whole range, the choice of a set of curves is by far more reasonable. Only the most linear, highest slope portion of each curve is selected for highest resolution measurements. A possible set of Q_l^m curves, resulting from the combination of six contrast curves (C_1, C_3, C_4, C_5, C_6 and C_7 in Fig. 3), is shown in Fig. 4 [21]: they cover the whole measurement range and present a high sensitivity. The evaluation of the unknown object point position S_p is performed by (i) setting the focal length to each selected value F_i , (ii) projecting the fringe patterns according to the MMP procedure, (iii) calculating the measured value $Q_{l,meas}^m$, (iv) inverting the corresponding calibration curve Q_l^m , and (v) evaluating it for $Q_l^m = Q_{l,meas}^m$. This procedure results in good measurement performances, as described in [21].

However, in the experimental practice, we realized that the number N_r of contrast curves that characterizes the calibration step was an issue. In fact, being the projection sequence formed by $N_p = 6$ patterns, the total amount N_T of patterns that must be projected was typically in the order of $N_r \cdot M_R / \Delta_S \cdot N_p = 6384$, and required a considerable amount of

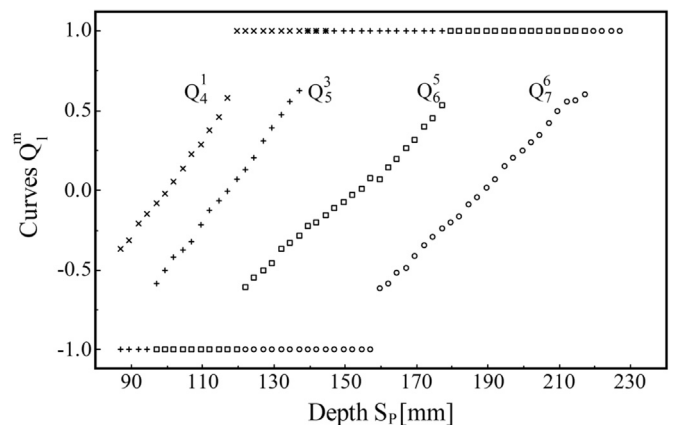


Fig. 4. Possible set of Q_l^m curves, resulting from the combination of six contrast curves (C_1, C_3, C_4, C_5, C_6 and C_7 in Fig. 3): $F_1 = 13.60$ mm; $F_3 = 13.88$ mm; $F_4 = 13.98$ mm; $F_5 = 14.29$ mm; $F_6 = 14.60$ mm; $F_7 = 14.93$ mm.

time. In addition, the number of contrast curves in the set of Q_l^m curves resulting from the selection criteria of the DCM approach was significantly lower than $N_r = 19$ (typical values being from 4 to 6). Finally, the selection of contrast curves C_l and C_m pairs was operator-dependent. For these reasons, we thought strategic to design an algorithm that automatically select the focal lengths that yield to the best combination between sensitivity and measurement range width. The algorithm, called *Automatic Focal Length Selection* (AFLS) runs before the calibration and significantly improves the efficiency of the system, as will be shown in the next section.

3. The AFLS algorithm

The AFLS algorithm has the scope of finding the minimal set of Q_l^m curves, each one defined in a sub-range of the whole depth measurement interval, having the highest linearity and the highest slope. Sub-ranges are adjacent to each other. The algorithm is presented with the aid of Fig. 5. Here, the whole depth measurement range spans from S_{MIN} to S_{MAX} and a single Q_l^m curve is considered in the sub-range S_1 - S_2 : its sigmoidal shape can be, in the first approximation, fitted with a straight line (L in the figure) passing by points $[S_1, -1]$ and $[S_2, 1]$. In correspondence to each depth value, the difference between the two curves can be quantified. The developed algorithm estimates the couple of focal lengths $[F_1, F_2]$ and the value of S_1 that (i) yield to a Q_2^1 curve with minimum distance from line L passing by points $[S_2, 1]$ and $[S_1, Q_2^1(S_1)]$, and (ii) maximizes the length $S_2 - S_1$ of the sub-range. The algorithm starts from $S_2 = S_{MAX}$.

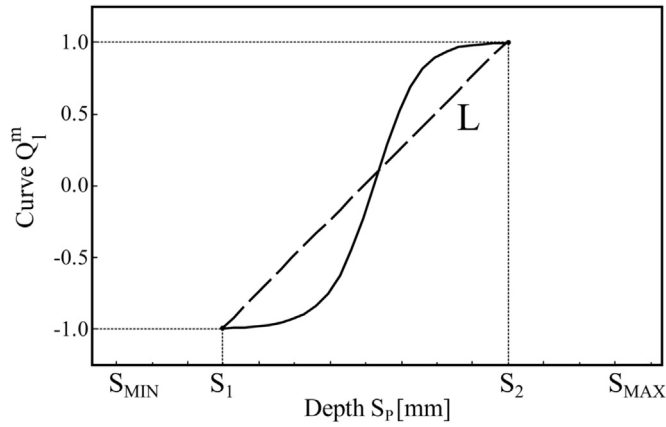


Fig. 5. Operation principle of the AFLS algorithm behavior. The solid line represents the curve Q_2^1 while the dashed line represents the straight line L passing by points $[S_1, -1]$ and $[S_2, 1]$.

3.1. Initial step

When $S_2 = S_{MAX}$ a fringe pattern is projected on a plane target, positioned at distance S_{MAX} , and the lens voltage is varied until the in-focus condition is detected. The corresponding focal length F_2 is determined by means of the following relation [21]:

$$F_2 = (V_2 \cdot 0.5052 + 39.69)^{-1} \tag{6}$$

where V_2 is the liquid lens supply voltage.

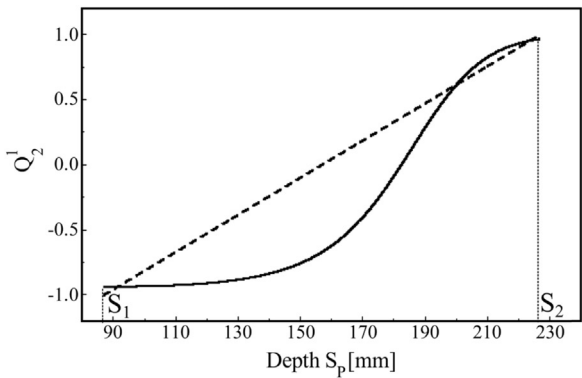
Then, the value of $Q_2^1(S_2)$ is set very close to 1 (a typical value is 0.95). Combining Eq. (5) and Eq. (2) yields the following expression:

$$Q_2^1(S_2) = \frac{e^{N_2} - e^{N_1}}{e^{N_2} + e^{N_1}} \tag{7}$$

where $N_2 = -\frac{1}{2} \cdot (\frac{\omega_2}{2\pi})^2 \cdot \sigma_2^2$, and $N_1 = -\frac{1}{2} \cdot (\frac{\omega_1}{2\pi})^2 \cdot \sigma_1^2$.

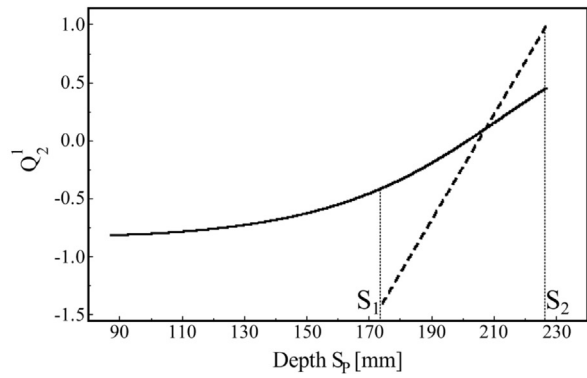
N_2 is evaluated using Eq. (4), for $S_p = S_2$ (parameter ω_2), and combining Eq. (3) and Eq. (1) for $F_r = F_2$, and $S_p = S_2$ (parameter σ_2). The value of N_1 is obtained inverting Eq. (7) with respect to N_1 :

$$N_1 = \ln \left(\frac{e^{N_2} \cdot (1 - Q_2^1(S_2))}{1 + Q_2^1(S_2)} \right) \tag{8}$$



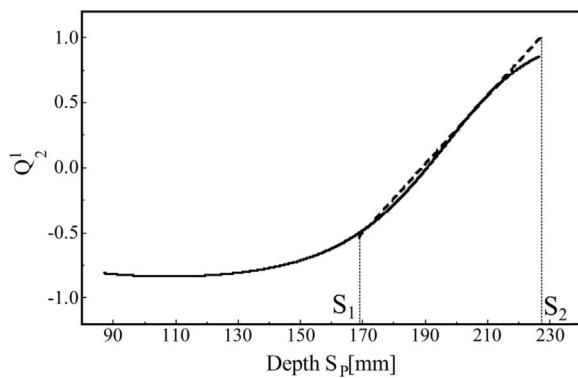
$S_2 = 227 \text{ mm}$ $S_1 = 87 \text{ mm}$ $E = 17.15 \text{ mm}$
 $F_2 = 14.93 \text{ mm}$ $F_1^0 = 14.49 \text{ mm}$
 $Q_2^1(S_2) = +1$ $Q_2^1(S_1) = -1$

(a)



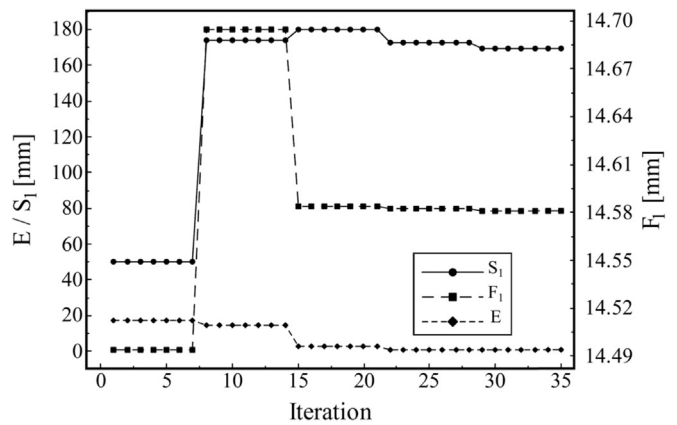
$S_1 = 174.13 \text{ mm}$ $E = 14.92 \text{ mm}$
 $F_1 = 14.71 \text{ mm}$
 $Q_2^1(S_1) = -0.40$

(b)



$S_1 = 169 \text{ mm}$ $E = 1.15 \text{ mm}$
 $F_1 = 14.60 \text{ mm}$
 $Q_2^1(S_1) = -0.54$

(c)



(d)

Fig. 6. Example of the parameters optimization using the AFLS algorithm. (a) Initial condition, (b) 10th iteration, (c) final (35th) iteration, and (d) values of parameters S_1 (• symbols, left vertical scale), F_1 (■ symbols, right vertical scale) and E (♦ symbols, left vertical scale) as a function of the number of iterations.

Table 1
Parameters evaluated by the AFLS optimization algorithm.

j	$[S_2]_j$ [mm]	$[F_2]_j$ [mm]	$[F_1^0]_j$ [mm]	$[S_1]_j$ [mm]	$[F_1]_j$ [mm]	$[Q_2^1(S_1)]_j$	$[V_2]_j$ [V]	$[V_1^0]_j$ [V]	$[V_1]_j$ [V]
1	227	14.93	14.49	169	14.60	-0.54	54	58	57
2	179	14.60	14.18	128	14.18	-0.50	57	61	61
3	138	14.18	13.69	96	13.79	-0.48	61	66	65
4	106	13.79	13.15	76	13.23	-0.51	65	72	71

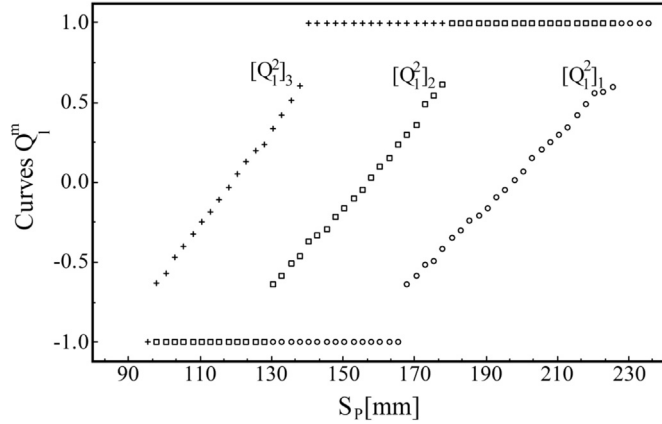


Fig. 7. Set of the experimental $[Q_2^1]_j$ curves resulting from the AFLS algorithm. $[F_2]_1 = 14.93$ mm; $[F_1]_1 = 14.60$ mm; $[F_1]_2 = 14.18$ mm; $[F_1]_3 = 13.79$ mm.

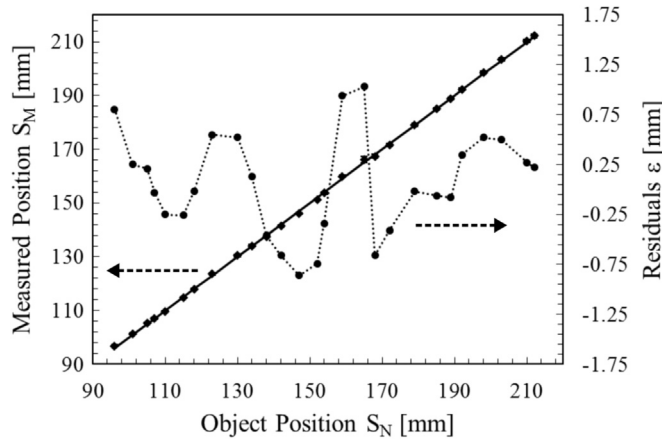


Fig. 8. Plot of the mean values of the measured positions S_M (♦ symbols, left vertical scale) with their standard deviations (bars), and of the residuals ϵ (• symbols, dashed line, right vertical scale) as a function of the nominal object position S_N , resulting from the AFLS based DCM approach. The solid line is the bisecting line. Dashed arrows indicate the reference vertical axis of each line.

Then, inverting Eq. (8) with respect to parameter σ_1 and using Eqs. (3) and (1) it is possible to derive the initial value of the focal length $F_r = F_1^0$ for which the contrast curve C_1 of Q_2^1 is almost zero at position S_2 .

3.2. Optimization step

The optimization step is performed for each depth sub-range. In this step, two equations are formed. The former has the following expression:

$$Q_2^r(S_p) = \frac{C_2(S_p) - C_r(S_p)}{C_2(S_p) + C_r(S_p)} \quad (9)$$

where curve $Q_2^r(S_p)$ is a function of both S_p and of the focal length F_r . Its value at S_2 is known, as well as focal lengths F_1^0 and F_2 derived from the procedure above. The latter expresses the equation of the straight line L

passing through points $[S_2, 1]$ and $[S_p, Q_2^r(S_p)]$; the initial values of S_p and $Q_2^r(S_p)$ are S_{MIN} and -1 respectively. The optimization step enters in a nonlinear least-squares iterative loop, based on a trust-region reflective algorithm [25], which finds the values $S_p = S_1$ and $F_r = F_1$ that minimize the sum of the squared differences (E) between the two curves and maximize the length of the sub-range $S_2 - S_1$. An example of the parameters optimization is given in Fig. 6.

Fig. 6.a plots curve Q_2^1 and line L at the initial condition. In this case $S_2 = S_{MAX}$, $S_1 = S_{MIN}$, values F_2 and F_1^0 , calculated by means of the procedure described in Section 3.1, are 14.93 mm and 14.49 mm respectively. Focal length F_1 equals F_1^0 . The slope of line L is 0.014 mm^{-1} and the value of E equals 17.15 mm.

Fig. 6.b shows curve Q_2^1 and line L at the 8th iteration. S_1 now equals 174.13 mm, $L(S_1)$ decreases to -1.40 , and the slope of line L increases to 0.045 mm^{-1} ; focal length F_1 increases to 14.71 mm, resulting in values $Q_2^1(S_1)$ and $Q_2^1(S_2)$ equal to -0.40 and 0.46 respectively. Curve $Q_2^1(S_p)$ shows its maximum linearity in the sub-range $S_1 - S_2$ and parameter E is reduced by 13% with respect to the initial value.

Fig. 6.c shows the $Q_2^1 - L$ pair at the last iteration (iteration 35). S_1 equals 169 mm, $L(S_1)$ equals -0.54 with a slope of 0.026 mm^{-1} . F_1 decreases to 14.60 mm and $Q_2^1(S_1)$ and $Q_2^1(S_2)$ equal -0.54 and 0.86 respectively. Curve Q_2^1 and line L optimally overlap and E reaches its minimum value (1.15 mm), corresponding to a reduction of 92% with respect to the previous one.

Fig. 6.d plots S_1 , F_1 and error E from the initial condition to the last iteration. It can be observed that the algorithm leaves the values of the parameters almost unchanged with respect to the initial condition of Fig. 6.a. in the first seven iterations. Then, S_1 and F_1 increase significantly, in an attempt to reduce the value of E . This results in the increment of the slope of line L and in the variation of the shape of curve Q_2^1 well evident in Fig. 6.b. The algorithm working point does not vary until iteration 14 and, then, the algorithm induces an abrupt change of F_1 , in order to find the best match between line L and curve Q_2^1 . In the subsequent iterations, the values of S_1 and F_1 are only slightly varied until the exit condition is reached. This occurs when the value of E in two subsequent iterations changes less than a threshold value. In this example, the threshold value is 1×10^{-6} mm.

3.3. Finding the next sub-range

The determination of the next sub-range is performed using the procedures described in Sections 3.1 and 3.2, provided that the parameters are suitably initialized. Labeling by index j the current sub-range, the initialization of the parameters is as follows:

$$[F_2]_j = [F_1]_{j-1} \quad (10)$$

$$[S_2]_j = [S_1]_{j-1} + S_C \quad (11)$$

In Eq. (11), S_C is a constant (typically the 10% of the sub-range $S_1 - S_2$) that is added to $[S_1]_{j-1}$ so that curves $[Q_2^1]_j$ and $[Q_2^1]_{j-1}$ are minimally overlapped. This solution does not influence the performances of the algorithm, but ensures that, at the borders of each sub-range, there is at least one Q_2^1 value to avoid lacks of measurement. The algorithm loops on index j and stops when either $[S_1]_j < S_{MIN}$ or $[V_1]_j > V_{MAX}$.

Table 1 shows the values of the parameters calculated by the AFLS algorithm over the measurement range from 87 to 227 mm (Fig. 4). For each j -th loop the input parameters S_2 , F_2 , and F_1^0 , and the output

parameters S_1 , F_1 and $Q_2^1(S_1)$ are presented. The voltage values required to set the focal lengths F_2 , F_1^0 and F_1 are listed in the last three columns of the table. At the beginning ($j=1$), S_2 equals S_{MAX} (as in Fig. 6.a) whilst in the subsequent loops it is initialized using Eq. (11). The algorithm stops at $j=3$, since the value $[V_1]_4$ is higher than V_{MAX} : hence, the focal length value $[F_1]_4 = 13.23$ mm can not be obtained. The resulting measurement range spans from 96 mm to 227 mm and is divided into three sub-ranges.

4. Experimental results and discussion

The optimization algorithm identifies four focal lengths, namely $[F_2]_1$, $[F_1]_1$, $[F_1]_2$, $[F_1]_3$. During the calibration of the system, only these values are used, and four contrast curves are obtained over the whole measurement range. With respect to the original procedure, the number N_T of projected patterns is reduced by 80%, with a significant improvement of the efficiency of the system. In terms of time, using a standard PC (*Intel i5 3.20 GHz 64 bit*, with *Windows 7* and *Labview 2014* installed) and a controlled slit (*Physik Instrumente MP37E*) to move the object plane, the calibration procedure takes about 112 s using the optimization algorithm, while it increases to 532 s without using it. The measuring time takes about 2 s using the optimization algorithm while it increases to 3 s with the non-optimized procedure.

Fig. 7 shows the $[Q_2^1]_j$ curves correspondingly derived. The experimental curves exhibit a high linearity (the linear regression coefficients R^2 is higher than 0.996). As already stated in [21], a difference between experimental and theoretical curves is the presence of noise. To avoid it, a threshold contrast value is required (in our case we used a threshold of 0.18). The insertion of a threshold results in abrupt discontinuities of $[Q_2^1]_j$ curves. This behavior is not critical for the measurement performances, since the experimental curves partially overlap and there is no “holes” in the depth range. The curves shown in Fig. 7 have been used to measure the depth S_p of object points belonging to a plane surface mounted on an automatically controlled slit, oriented along the system optical axis, and evaluating depth maps corresponding to focal lengths $[F_2]_1$, $[F_1]_1$, $[F_1]_2$, $[F_1]_3$ at known positions S_N in the selected depth range. The results are shown in Fig. 8 where full diamonds (left vertical scale) and bars represent the average S_M values with their standard deviations, as a function of known S_N values. Full dots (right vertical scale) represent the residuals ε_i , i.e. the difference between the means of the measured points and the nominal object plane position. The solid line is the bisecting line. The residuals are uniform in the whole measurement range with a maximum value of 1.06 mm.

The σ_0 was computed with a linear regression over all the measured points. The linearity of the measurements in the selected range is excellent ($R^2 = 0.9998$) with a $\sigma_0 = 0.73$ mm over a depth range of about 131 mm, which corresponds to the 0.55% of the range. These values are in agreement with those observed for the original DCM approach [21].

The comparison of this approach with other triangulation-based setups with two or more optical imaging systems highlights the robustness against shadows and occlusions induced errors. However, being the triangulation base of our system reduced at the dimension of the lens aperture [26], the measurement resolution is lower with respect to that obtainable using a triangulation-based system (see for example the one described in [27]).

5. Conclusions

In this paper, we demonstrated that the AFSL algorithm, consisting in the identification of optimal contrast curve pairs through focal length changes in the detection objective of a DFD setup, yields increased efficiency of the system (up to 80% in terms of time) as compared to the non-optimized DCM approach. Measurement errors as low as 0.73 mm (corresponding to 0.55% of the depth range) are achieved over a range of more than 130 mm. This was obtained using a simple and compact

setup, without moving parts, with a single camera/illuminator coaxial assembly, the illuminator being telecentric and the camera being equipped with a liquid lens, variable-focus objective. This opens perspectives for the use of this method in industrial and/or biomedical vision instrumentation.

Acknowledgements

We wish to thank Mr. Gabriele Coffetti for his precious support in the experimental activities.

References

- [1] Liliensblum E, Al-Hamadi A. A structured light approach for 3-D surface reconstruction with a stereo line-scan system. *IEEE Trans Instrum Meas* 2015;65:1266–74.
- [2] Anchini R, Di Leo G, Liguori C, Paolillo A. A new calibration procedure for 3-D shape measurement system based on phase shifting projected fringe profilometry. *IEEE Trans Instrum Meas* 2009;58:1291–8.
- [3] Sansoni G, Cattaneo C, Trebeschi M, Gibelli D, Porta D, Picozzi M. Feasibility of contactless 3D optical measurement for the analysis of bone and soft tissues lesions: new technologies and perspectives in forensic sciences. *J Forensic Sci* 2009;54:540–5.
- [4] Tognola G, Parazzini M, Ravazzani P, Grandori F, Svelto C. 3-D acquisition and quantitative measurements of anatomical parts by optical scanning and image reconstruction from unorganized range data. *IEEE Trans Instrum Meas* 2003;52:1665–73.
- [5] Sansoni G, Docchio F. In-field performance of an optical digitizer for the reverse engineering of free-form surfaces. *Int J Adv Manuf Tech* 2005;26:1353–61.
- [6] Shaffer M, Große M, Harendt B, Kowarschik R. Outdoor three-dimensional shape measurements using laser-based structured illumination. *Opt Eng* 2012;51:090503.
- [7] Große M, Shaffer M, Harendt B, Kowarschik R. Fast data acquisition for three-dimensional shape measurement using fixed-pattern projection and temporal coding. *Opt Eng* 2011;50:100503.
- [8] Guan C, Hassebrook LG, Lau DL. Composite structured light pattern for three-dimensional video. *Opt Exp* 2003;11(5):406–17.
- [9] Wang Y, Zhang S. Superfast multifrequency phase-shifting technique with optimal pulse width modulation. *Opt Exp* 2011;19:5149–55.
- [10] Takeda M, Gu Q, Kinoshita M, Takai H, Takahashi Y. Frequency-multiplex Fourier transform profilometry: a single-shot three-dimensional shape measurement of object with large height discontinuities and/or surface isolations. *Appl Opt* 1997;36(22):5347–54.
- [11] Zhong J, Zhang Y. Absolute phase-measurement technique based on number theory in multifrequency grating projection profilometry. *Appl Opt* 2001;40(4):492–500.
- [12] Choudhury D, Takeda M. Frequency-multiplexed profilometric phase coding for three-dimensional object recognition without 2pi phase ambiguity. *Opt Lett* 2002;27(16):1466–8.
- [13] Liu W, Wang Z, Mu G, Fang Z. Color-coded projection grating method for shape measurement with a single exposure. *Appl Opt* 2000;39(20):336–42.
- [14] Pages J, Salvi J, Collewet C, Forset J. Optimized de Bruijn patterns for one-shot shape acquisition. *Imag Vis Comp* 2005;23(8):707–20.
- [15] Dou Y, Su X. A flexible 3-D profilometry based on fringe contrast analysis. *Opt Lasers Tech* 2012;44:844–9.
- [16] Dou Y, Su X, Chen Y, Wang Y. A flexible fast 3-D profilometry based on modulation measurement. *Opt Lasers Eng* 2011;49:376–83.
- [17] Wang Y, Su X, Dou Y. A fast three-dimensional object recognition based on modulation analysis. *Opt Las Eng* 2010;48:1027–33.
- [18] Yoshizawa T, Shinoda T, Otani Y. Uni-axis range finder using contrast detection of a projected pattern. *Proc SPIE* 2001;4190:115–22.
- [19] Zhipan H, Zhenzhong L, Quifeng W, Lifang F. A novel approach to recovering depth from defocus. *Sens Transducers* 2013;160:36–41.
- [20] Fuentez-Fernandez J, Cuevas S, Alvarez-Nunez LC, Watson A. Tests and evaluation of a variable focus liquid lens for curvature wavefront sensors in astronomy. *Appl Opt* 2013;52:7256–64.
- [21] Pasinetti S, Bodini I, Lancini M, Docchio F, Sansoni G. A depth from defocus measurement system using a liquid lens objective for extended depth range. *IEEE Trans Instrum Meas* 2017;66:441–50.
- [22] Chaudhuri S, Rajagopalan AN. Depth recovery from defocused images. In: *Depth from defocus: a real aperture imaging approach*, New York: Springer-Verlag; 1999, p. 14–27.
- [23] Su L, Su X, Li W, Xiang L. Application of modulation measurement profilometry to objects with surface holes. *Appl Opt* 1999;38:1153–7.
- [24] Subbarao M. Depth recovery from blurred edges. In: *Computer Vision and Pattern Recognition, CVPR '88 Ann Arbor, MI, USA, 5–9 June 1988*.
- [25] Coleman TF, Li Y. An interior, trust region approach for nonlinear minimization subject to bounds. *SIAM J Optim* 1996;6(2):418–45.
- [26] Schechner YY, Kiryati N. Depth from defocus vs stereo: how different really are they? *Int J Comput Vis* 2000;39:141–62.
- [27] Biancardi L, Sansoni G, Docchio F. Adaptive whole field optical profilometry: a study of the systematic errors. *IEEE Trans Instrum Meas* 1995;44:36–41.



Simone Pasinetti received the B.S. degree and the M.S. degree (with honors) in Automation Engineering from University of Brescia, Brescia, Italy, in 2009 and 2011 respectively. He received the Ph. D. degree in applied mechanics from University of Brescia, Brescia, Italy, in 2015. During the Ph. D. he had in contact with the Institute of Intelligent Systems and Robotics (ISIR), Paris, France, where he carried out research concerning the dynamic posture analysis. Since January 2015, he has been a research fellow for the Optoelectronics Laboratory (OPTOLAB) in the Department of Information Engineering at University of Brescia, Brescia, Italy.



Prof. Franco Docchio received his M.S. Degree in 1976. He worked at the Centro di Elettronica Quantistica of Italy between 1978 and 1987, where he carried out research concerning laser development, laser applications in industry and bio-medicine and laser-tissue interaction. In 1987 he joined the Dipartimento di Elettronica per l'Automazione of the University of Brescia, where he presently holds the Full Professorship in Electrical Measurements. Prof. Docchio, author of more than 250 publications, is a member of the Laboratory of Optoelectronics. He is currently Fellow of the European Optical Society. He is the Director of the National Journal "Tutto_Misure".



In March 2006 **Ileana Bodini** received her master's degree in Mechanical Engineering. In April 2010 she received her Ph.D. in Sciences, Technologies and Measurements for Space - Mechanical Measurement for Engineering (University of Padua). Since 2007 she has joined the group of Mechanical and Thermal Measurement of the university of Brescia. Since September 2014 she has worked for the Laboratory of Optoelectronics (University of Brescia) and her principal research topics are: (i) design vision systems (2D and 3D) for research and industrial applications; (ii) development of measurement devices based on vision systems; (iii) techniques for data analysis, measurements and diagnostic.



Prof. Giovanna Sansoni received her degree in Electronic Engineering at the Politecnico of Milan, Italy, in 1984. In 1985 she joined the University of Brescia, Italy. She is now Full Professor of Electrical Measurements at the Department of Information Engineering of the University of Brescia. Her research interests are in the 3D vision area. Among these are the implementation of camera and projector calibration for the absolute measurement of shape in active stereo vision systems; the development of light coding methods for whole-field optical profilometry; the application of optical instrumentation to the acquisition and the reverse engineering of free-form surfaces.



Matteo Lancini received the master's degree in mechanical engineering in 2005 from the University of Brescia. He was a research contractor with the Department of Industrial and Mechanical Engineering, University of Brescia, Brescia, Italy, where he was involved in the development of measurement techniques for industrial diagnostics, and focused on measurements in uncontrolled environments from 2005 to 2009. He received his PhD degree in Applied Mechanics from the University of Brescia in 2015. He is currently an Assistant Professor with the Mechanical and Thermal Measurements Laboratory, Department of Industrial and Mechanical Engineering, University of Brescia.